PAPER

Check for updates

Biogenically forged ZnO nanoparticles using *Salvia hispanica* L. microgreens for their potential antimicrobial activity towards food-borne pathogens

Baru Venkata Naga Sahithi and Vasantha Veerappa Lakshmaiah (ID) *

Microgreens have been extensively researched because of their dense nutritional content and high concentration of health-promoting and therapeutic bioactive compounds. Simultaneously, green synthesis of nanoparticles has emerged as a biogenic and sustainable approach for nanomaterial preparation using plant extracts as reducing and stabilizing agents. In the current study, zinc oxide nanoparticles (ZnO NPs) were synthesized using phytochemically enriched extracts of chia (*Salvia hispanica*) microgreens. The synthesis of ZnO NPs was systematically optimized, and the resulting nanomaterials were characterized using UV-Visible spectroscopy, XRD, FTIR, SEM, DLS, and TEM to confirm their structural, morphological, and physicochemical properties. The characterization results confirmed the successful formation of ZnO NPs with a crystalline size of 79.4 nm and a zeta potential of -42.2 ± 0.29 mV, indicating good stability and uniformity. To further explore the bioactivity, *in silico* molecular docking was performed to investigate the interactions between chia-derived phytochemicals and key receptors of food-borne pathogens *Aeromonas caviae* and *Staphylococcus pasteuri* isolated from chicken meat. Based on these insights, the antimicrobial activity of MG-ZnO NPs (Microgreen-derived zinc oxide nanoparticles) was evaluated. The nanoparticles exhibited notable antibacterial activity, with greater effectiveness against *S. pasteuri*. MIC values for *S. pasteuri* and *A. caviae* were found to be 62.5 μg mL^{-1} and 250 μg mL^{-1}, respectively, while the corresponding MBC values were 125 μg mL^{-1} and 500 μg mL^{-1}. The MBC/MIC ratios confirmed the bactericidal nature of MG-ZnO NPs against both strains. These findings highlight the potential of chia microgreen-derived ZnO nanoparticles as promising antimicrobial agents for combating foodborne pathogens.

1 Introduction

Foodborne diseases continue to remain a major global public health concern, affecting millions annually due to the consumption of contaminated food. These illnesses are primarily caused by microbial pathogens that can enter the food supply at any stage—production, processing, or distribution. Meat and dairy products are particularly vulnerable and have been identified as significant sources of foodborne infections.[1] Global meat production has risen sharply since 1961, with Asia leading the surge, especially in poultry consumption.[2] However, this increase correlates with a rise in meat-associated diseases. The microbial safety of meat depends on animal health and hygiene during slaughter, processing, and retail.[3] Contamination may result from infected animals or poor sanitary practices post-slaughter. Common meat-borne pathogens include *Staphylococcus aureus*, *E. coli*, *Salmonella* spp., and *Bacillus*

cereus.[4] Recently, *Aeromonas caviae* and *Staphylococcus pasteuri* have emerged as notable contaminants in meat. *A. caviae*, a Gram-negative bacterium from aquatic environments, is linked to gastrointestinal infections and often contaminates meat during handling.[5,6] *S. pasteuri*, a coagulase-negative Gram-positive bacterium, though less common, has been associated with infections such as bacteremia and UTIs.[7–9] Alarmingly, some *S. pasteuri* strains exhibit antibiotic resistance, raising concerns for food safety and public health.[10] Antibiotic resistance is a serious global problem, as many microbes can quickly adapt and become resistant to drugs.[11] Because of this, there is a growing need for alternatives to traditional antibiotics. One promising option is the use of natural plant-based compounds, which can fight a wide range of microbes with a lower chance of causing resistance.[12]

Over the past decade, pseudocereals such as chia (*Salvia hispanica*), quinoa (*Chenopodium quinoa*), and amaranth (*Amaranthus* spp.) have attracted considerable attention from the research community due to their exceptional nutritional and therapeutic potential.[13] This growing interest is largely

Department of Life Sciences, CHRIST (Deemed to be University), Bangalore-560029, India. E-mail: vasantha.vl@christuniversity.in

attributed to their naturally gluten-free nature and enriched phytochemical profile, which includes polyphenols, flavonoids, phenolic acids, saponins, phytosterols, and betalains. Among them, chia seeds have been extensively studied for their high content of protein, dietary fiber, essential vitamins, minerals, and omega-3 fatty acids.[14] While the medicinal and nutritional properties of chia seeds are well documented, there remains limited research on the bioactive composition and functional attributes across different growth stages of chia.[15] Notably, recent findings suggest that chia microgreens possess a more concentrated and enhanced phytochemical profile compared to other developmental stages.[16] Exploring these phytochemically enriched microgreens into the green synthesis of nanomaterials may further amplify the biological activity of the resulting nanoparticles, offering promising applications in medicine, food safety, and nanobiotechnology.[17]

In a previous study, Singh *et al.* successfully synthesized zinc oxide nanoparticles (ZnO NPs) using chia seed extract and demonstrated their antibacterial efficacy against *Staphylococcus aureus*, a multidrug-resistant pathogen.[18] Building on this approach, the current study investigates the phytochemical profile of chia microgreen extract using LC-MS analysis and employs *in silico* molecular docking to evaluate the antimicrobial potential of the identified phytochemicals. Based on these insights, chia microgreens were utilized as a green reducing and stabilizing agent for the biofabrication of ZnO nanoparticles, which were subsequently evaluated for their antibacterial activity against emerging foodborne pathogens such as *A. caviae* and *S. pasteuri*.

2 Materials and methods

2.1 Preparation of extract and characterization

Chia microgreens were grown in pots using cocopeat as the growth medium. They were regularly monitored and harvested once the first set of true leaves appeared. For extraction, 10 grams of dried microgreens were dried at 40 °C and macerated using 100 mL of distilled water and heated at 80 °C for 4 hours. The resulting extract was then filtered using Whatman no. 1 filter paper, and the filtered extract was stored at 4 °C. The extract was further analysed using LC-MS to identify the phytochemicals present.[19]

2.2 Optimization of parameters for the synthesis of MG-ZnO NPs

MG-ZnO NPs synthesis was optimized by assessing the influence of four key physicochemical parameters: metal precursor concentration, pH, incubation time, and the ratio of plant extract to metal solution. Zinc acetate concentrations of 0.01 M to 0.2 M were tested, along with a pH gradient from 2 to 14. Further, a fixed 50 mL of zinc acetate solution was mixed with varying volumes of plant extract. Additionally, different incubation periods (2, 4, 6, and 8 hours) were examined. The ideal parameters for nanoparticle synthesis were determined based on characterization results obtained through UV-Vis

spectroscopy, dynamic light scattering (DLS), and X-ray diffraction (XRD) analyses.

2.3 Synthesis of MG-ZnO NPs

The green synthesis of metallic nanoparticles is dependent on many key factors like pH, precursor concentration, and incubation time. Based on optimized conditions, equal volumes of 0.15 M zinc acetate solution and plant extract were mixed, and the pH was brought to 11 by gradual addition of 1 M NaOH. The mixture was stirred at 80 °C for six hours to facilitate nanoparticle formation. After the reaction, the solution was centrifuged at 10 000 rpm to obtain the nanoparticles, and the pellet was dried overnight in a hot air oven at 50 °C to obtain MG-ZnO NPs.

2.4 Characterization of MG-ZnO NPs

MG-ZnO NPs synthesis was confirmed through a series of characterization techniques. UV-Vis spectroscopy was employed to analyse the optical properties and confirm nanoparticle formation. Fourier Transform Infrared (FTIR) spectroscopy, conducted in the 4000–400 cm^{-1} range, was used to identify functional groups present on the surface of the nanoparticles. The crystalline structure was determined from powder X-ray Diffraction (XRD) data, while Dynamic Light Scattering (DLS) was used to assess the particle size distribution and surface charge. Additionally, the morphology and size of the nanoparticles were examined using Scanning Electron Microscopy (SEM) and Transmission Electron Microscopy (TEM).

2.5 Isolation and characterization of microorganisms

Microorganisms used in this study were isolated from the large intestine and fecal samples of chickens collected during the slaughtering process. The samples were surface sterilized and macerated in 0.9% saline solution to maintain isotonic conditions. Serial dilutions were prepared, and the diluted suspensions were spread on LB agar plates, followed by incubation at 37 °C to facilitate the growth of distinct bacterial colonies. The pathogenic potential of the isolates was preliminarily screened using haemolysis assays. Pathogenic strains were further identified through 16S rRNA gene sequencing.[20] Genomic DNA was extracted, and the 16S rRNA gene was amplified using universal primers 16SrRNA-F and 16SrRNA-R. Bidirectional sequencing was carried out using the same primers with the BDT v3.1 Cycle Sequencing Kit on an ABI 3730xl Genetic Analyzer. A consensus sequence was generated from forward and reverse reads using aligner software and analyzed using the NCBI BLAST tool. The top ten closely related sequences were aligned using ClustalW, and a phylogenetic tree was constructed using MEGA version 10 to determine the evolutionary relationship of the isolates.

2.6 *In silico* studies

Computational docking studies of *Salvia hispanica*-derived phytochemicals were carried out using AutoDock Vina integrated within UCSF Chimera. The 3D structures of the ligands identified from LCMS were retrieved from the PubChem

database, while the crystal structures of the target proteins, transglycosylase and propyl endopeptidase, were obtained from the RCSB Protein Data Bank with PDB IDs 3VMQ and 3IUJ, respectively. Docking simulations were performed to evaluate binding affinities (kcal mol^{-1}), and the ligand–protein complexes exhibiting the highest binding scores were further studied. Key molecular interactions, including hydrogen bonding and hydrophobic contacts, were visualized and interpreted using Discovery Studio Visualizer v21.1.0.20298.[21]

2.7 Antimicrobial assay of MG-ZnO NPs

Following the *in silico* molecular docking studies, experimental validation was performed to evaluate the antimicrobial efficacy of the green-synthesized MG-ZnO nanoparticles (NPs). The minimum inhibitory concentration (MIC) and minimum bactericidal concentration (MBC) were determined using the broth microdilution method, following the Clinical and Laboratory Standards Institute (CLSI) guidelines with slight modifications. A two-fold serial dilution of the nanoparticle stock solution was prepared, ranging from 1000 μg mL^{-1} to 15.62 μg mL^{-1}. The assay was conducted in a 96-well plate. Each well received 100 μL of the nanoparticle solution at the specific concentration, 100 μL of sterile LB medium, and 20 μL of bacterial suspension adjusted to 10^6 CFU mL^{-1}. The bacterial suspension with LB broth, without the nanoparticle suspension, was taken as the negative control, while a standard antibiotic control (Ampicillin, 1 mg mL^{-1}) was included as a positive control for antimicrobial activity. The plates were incubated at 37 °C for 24 hours. Bacterial growth was assessed by measuring the optical density at 600 nm (OD$_{600}$). MIC was defined as the lowest concentration of nanoparticles that showed no visible turbidity and an OD$_{600}$ reading comparable to that of the standard antibiotic. To determine the MBC, an aliquot of 50 μL was aseptically taken from each well showing no visible growth and streaked onto LB agar plates. These plates were incubated at 37 °C for 24 hours. The MBC was defined as the lowest concentration of nanoparticles at which no bacterial colonies appeared on the agar, indicating bactericidal activity.[22]

2.8 Statistical analysis

All the tests were performed in triplicate to reduce the handling error and statistically analysed using SPSS by applying one-way ANOVA over the data. The standard deviation was also determined using IBM SPSS statistics v26 2019 and is represented as error bars. All the data were given as means ± standard deviation.

3 Results and discussion

3.1 Characterization of plant extract

LC-MS analysis of chia microgreens extract was performed to identify the bioactive phytochemicals present in the sample. The resulting chromatogram (Fig. S1) revealed a diverse range of bioactive compounds, including flavonoids, phenolic acids, terpenoids, and other aromatic compounds. A total of 32 compounds were identified (Table S1). These identified phytochemicals were further used as ligands in molecular docking

studies to assess their interactions with bacterial target proteins. FTIR graph (Fig. S2) of the plant extract has peaks representing C=C, C–O, C–N, C=O, C=C, C–C, C–H, N–H, and O–H groups, which aligns with the LCMS data.

3.2 Optimization and characterization of MG-ZnO NPs

3.2.1. UV-Vis Spectral analysis. The formation of zinc oxide nanoparticles was confirmed through UV-Vis spectroscopy with absorption maxima of 362 nm (Fig. 3(a)), and the synthesis conditions were optimized by zinc acetate concentration, ratio of plant extract to zinc acetate solution, pH, and incubation time. As the zinc acetate concentration increased, the absorption intensity increased, showing sharper peaks with increased nucleation. The sharpest and narrowest peak was observed at 0.15 M, indicating the optimal nanoparticle formation. However, concentration beyond 0.15 M resulted in broadening of the peak (Fig. 1(a)), due to particle aggregation caused by the presence of excess metal ions.[23] In the extract-to-metal ratio study (Fig. 1(b)), various volumes of plant extract were used with a fixed amount of metal ion solution (50 mL). Increasing the volume of plant extract led to higher absorption because of the presence of a high amount of reducing and capping agents, facilitating effective nucleation and stabilization. Beyond this point, the intensity decreased, possibly due to excess capping agents interfering with proper nucleation. To further optimize the synthesis, the effect of pH on nanoparticle formation was studied across a range of 2 to 14. No significant absorption peak at 362 nm was detected till pH 10 (Fig. 1(c)), but a strong peak was observed at pH 11, indicating optimal nanoparticle formation. At pH values above 11, the peak intensity declined, possibly due to reduced power of phenolic groups caused by increasing OH$^-$ ion-induced resonance stabilization.[24] Lastly, the influence of incubation time was assessed. The highest absorption peak was observed at 6 hours, providing a high absorption peak, suggesting the formation of uniform particles (Fig. 1(d)), while the incubation period time shorter or longer than 6 hours resulted in reduced absorption peak, suggesting incomplete formation or instability due to insufficient reaction time or particle overgrowth and aggregation.[25]

3.2.2 Powder X-ray diffraction (XRD) analysis. The crystalline nature and microstrain of the synthesized nanoparticles were confirmed through X-ray diffraction (XRD) analysis. In addition to UV-Vis spectroscopy, XRD was employed to optimize both zinc acetate concentration and plant extract-to-metal solution ratio. At lower concentrations, the XRD patterns exhibited broad and less intense peaks, indicating the high microstrain and poor crystallinity (Fig. 2(a)). As the concentration increased, the diffraction peaks became sharper and intense, indicating proper crystallinity and reduced microstrain. However, at concentrations beyond the optimum concentration (0.15 M), peaks broadening and increased microstrain were reappeared likely due to nanoparticle aggregation.[26] A similar trend was noted with the extract-to-metal solution ratio. The 1 : 1 ratio produced the most prominent and well-defined XRD peaks, with minimal microstrain indicating stable and well-formed crystals (Fig. 2(b)). The optimized
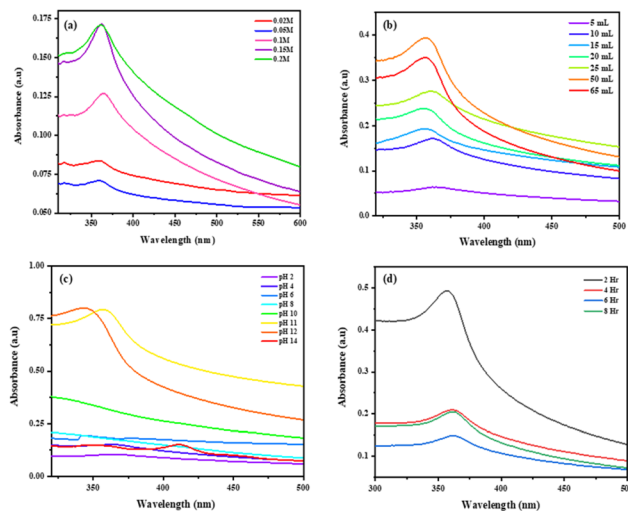
Fig. 1 The UV-Vis Spectra of Optimization studies of four parameters (a) concentration of zinc acetate (b) ratio of plant extract and zinc acetate solution (c) pH (d) incubation time.
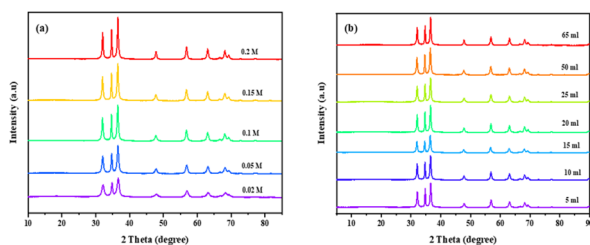

Fig. 2 XRD graphs of optimization studies of (a) concentration of zinc acetate (b) plant extract to metal solution ratio.

nanoparticles exhibited distinct diffraction peaks at 2θ values of 32.07°, 34.46°, 36.53°, 47.79°, 57.16°, 63.10°, 67.07°, 68.49°, 69.77°, 72.67°, 77.64°, and 81.65 corresponding to (1 0 0), (0 0 2), (1 0 1), (1 0 2), (1 1 0), (1 0 3), (2 0 0), (1 1 2), (2 0 1), (0 0 4), (2 0 2), (1 0 4), lattice planes respectively (Fig. 3(b)). At optimized conditions, the diffraction peaks at 2θ values of 32.07°, 34.46°, 36.53° with lattice parameters (1 0 0), (0 0 2), (1 0 1), (1 0 2) showed sharp and intense peaks, contributing to the crystallinity nature of MG-ZnO NPs. These peaks matched the standard JCPDS (Joint Committee on Powder Diffraction Standards) card number 96-101-1259, confirming the formation of MG-ZnO NPs.

The Debye–Scherrer equation was used to calculate the average crystalline size.

$$D = \frac{0.9\lambda}{\beta \cos\theta}$$

where, D represents the crystalline size, λ is the X-ray wavelength (1.54 A⁰), β represents the full width at half maximum of the peak in radians, and θ is the Bragg angle. The microstrain of the sample was calculated using the equation.
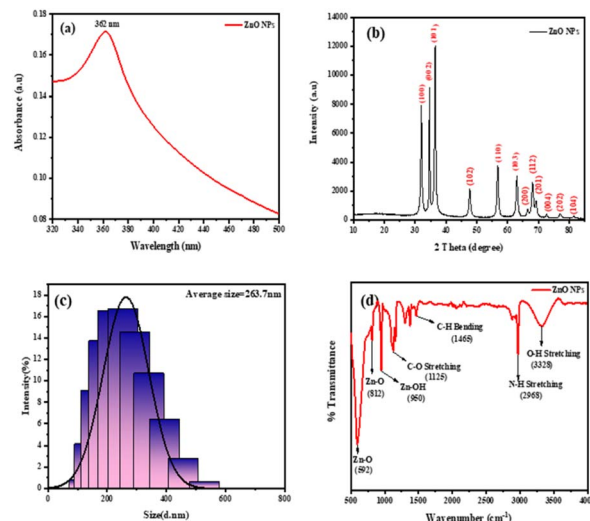
$$\varepsilon = \cdot \frac{\beta}{4 \tan\theta}$$

Fig. 3 Characterization of optmized MG-ZnO NPs (a) UV-Vis spectra of MG-ZnO NPs (b) XRD graph of MG-ZnO NPs (c) average particle size of MG-ZnO NPs (d) FTIR graph of MG-ZnO NPs.

where ε represents the microstrain, β is the full width at half maximum of the peak in radians, and θ is the Bragg's angle. The average crystalline size and the microstrain of the optimized MG-ZnO NPs were found to be 74.18 nm and 0.00247, respectively.

3.2.3 Dynamic light scattering (DLS) analysis. Dynamic light scattering analysis was conducted to further optimize the nanoparticles synthesis parameters by evaluating the particle size distribution and stability of the MG-ZnO NPs. As the concentration of the zinc acetate increased, a noticeable decrease in both average particle size and zeta potential was observed. The most uniform and well-defined particles were obtained at the optimal concentration of 0.15 M, indicating efficient and controlled nucleation. Similarly, the effect of plant extract volume was studied, where at lower volumes (5 mL, 10 mL, 15 mL) the nanoparticles exhibited larger sizes and lower zeta potentials, suggesting poor stabilization due to insufficient amount of phytochemicals for effective capping. Although the zeta potential improved at 20 mL and 25 mL, the particle size remained unstable, likely due to partial agglomeration caused by intermediate capping efficiency. At 50 mL, the smallest particle size (263.71 ± 1.4 nm), with a PdI value of 0.265 and the highest zeta potential (−42.2 ± 0.29) were recorded, indicating optimal stabilization and confirming the ideal plant extract-to-metal solution ratio as 1 : 1 (Fig. 3(c)). Further increase in plant extract led to a slight increase in particle size and reduced zeta potential, possibly due to the presence of excessive capping agents which interfere with proper nucleation.[27] Lastly, the effect of the incubation time revealed that 6 hours resulted in the smallest particle size compared to other incubation time durations.

3.2.4 Fourier Transform Infrared spectroscopy (FTIR) analysis. FTIR spectroscopy was conducted to identify the functional the plant extract responsible for stabilizing the nanoparticles. The formation of MG-ZnO NPs was confirmed by
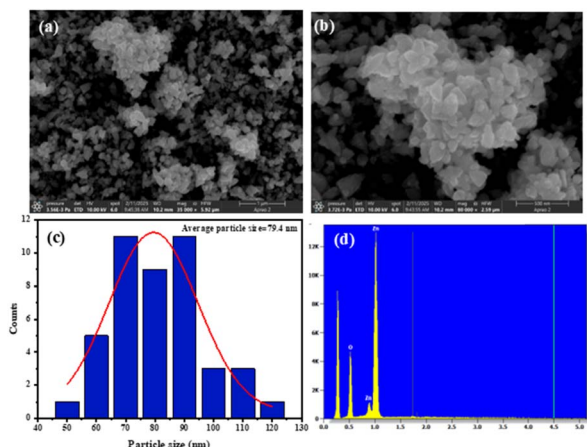
Fig. 4 SEM images of MG-ZnO NPs (a) MG-ZnO NPs at 1 μm (b) MG-ZnO NPs at 500 nm (c) histogram of particle size distribution (d) EDX graph of MG-ZnO NPs.
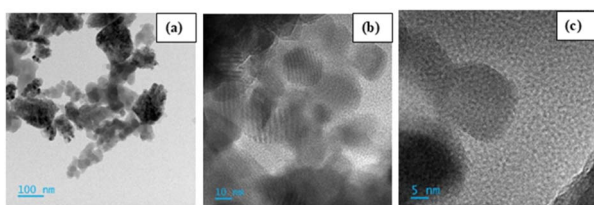

Fig. 5 TEM images of MG-ZnO NPs (a) MG-ZnO NPs at 100 nm scale (b) MG-ZnO NPs at 10 nm (c) MG-ZnO NPs at 5 nm.

the presence of peaks 947 cm^{-1}, 814 cm^{-1}, and 616 cm^{-1} (Fig. 3(d)) corresponding to Zn–OH, Zn–O, and Zn–O, respectively.[28] Additionally, the FTIR spectrum displayed peaks at 3312 cm^{-1} (O–H stretching), 2973 cm^{-1} (N–H stretching), 1466 cm^{-1} (C–H bending), and 1117 cm^{-1} (C–O stretching), indicating the presence of phytochemicals that likely contributed to nanoparticle formation and stability.[29] Notably, the presence of N–H groups not only assists in the reduction of metal ions but also enhances the antimicrobial property of the MG-ZnO NPs.

3.2.5 SEM analysis. The morphological characteristics of the synthesized nanoparticles were examined using Scanning Electron Microscopy (SEM). Under optimized synthesis

conditions, the MG-ZnO NPs exhibited a pyramid shape (Fig. 4(a) and (b)), which was similar to the reported shapes of ZnO NPs.[30] The average particle size was found to be 79.4 nm (Fig. 4(c)). To verify the elemental composition, Energy Dispersive X-ray (EDX) analysis was performed. The EDX spectrum (Fig. 4(d)) displayed prominent peaks corresponding to zinc (Zn) and oxygen (O), confirming the presence of ZnO nanoparticles with high purity. Furthermore, elemental mapping analysis showed a uniform distribution of zinc and oxygen throughout the sample, supporting the composition of the synthesized nanoparticles.

3.2.6 TEM analysis. The Transmission Electron Microscopy (TEM) study was carried out to investigate further details about the green-synthesized MG-ZnO NPs at the nanoscale. TEM images at different scales (Fig. 5(a)–(c)) confirmed that the green synthesized MG-ZnO NPs possess a polycrystalline hexagonal structure, with particle size ranging between 70–80 nm, closely aligning with the measurements obtained from XRD analysis.

The average particle size of MG-ZnO nanoparticles (NPs) was observed to range between 70–80 nm based on TEM analysis, while SEM showed an average size of approximately 79.4 nm. However, DLS analysis revealed a significantly larger hydrodynamic diameter of around 263.71 nm. This discrepancy can be attributed to the tendency of nanoparticles to aggregate in suspension, which is commonly detected in DLS measurements due to the presence of solvent layers and interparticle interactions in the colloidal state. The characterization of optimized MG-ZnO NPs has been summarized (Table 1).

3.3 Mechanism of MG-ZnO NPs formation

The ZnO NPs synthesis using chia microgreens is driven by the redox activity of phytochemicals, particularly phenolic compounds. Under alkaline conditions, these polyphenolic compounds undergo tautomerization, releasing electrons, which facilitate the reduction of zinc ions (Zn^{2+}) to metallic zinc (Zn^{0}). The metal ions then undergo spontaneous oxidation to form ZnO NPs (Fig. 6).[31]

3.4 Stability studies

The stability studies of the green synthesized MG-ZnO NPs were evaluated under various conditions, including different pH

Table 1 Characterization of optimized MG-ZnO NPs

| S.No	Characterization technique	Inference
1	UV-Vis	A narrow peak was observed at 362 nm, which confirms the formation of MG-ZnO NPs
2	FTIR	Confirmed the presence of phytochemicals on the surface of MG-ZnO NPs
3	XRD	The peaks matched the standard JCPDS card number 96-101-1259, confirming the formation of MG-ZnO NPs
4	DLS	The average particle size and zeta potential of MG-ZnO NPs in the solution were found to be 263.71 ± 1.4 nm and −42.2 ± 0.29, respectively, with a PdI value of 0.265
5	SEM	The average particle size of MG-ZnO NPs was found to be 79.4 nm
6	TEM	The images of MG-ZnO NPs confirmed the polycrystalline hexagonal structure, with particle size ranging between 70–80 nm
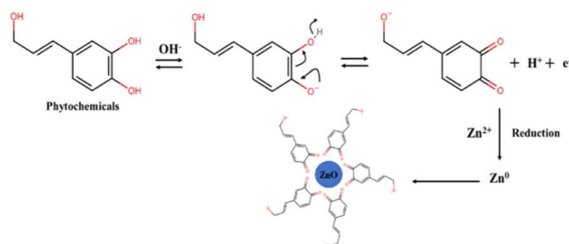
Fig. 6 Schematic representation of MG–ZnO NPs formation.

ranges, NaCl concentrations, and storage durations. All the experiments were carried out in triplicate. The statistical analysis was performed using one-way ANOVA, and the results revealed no significant difference between the replicates ($p < 0.05$), confirming the consistency and reproducibility.

3.4.1 Effect of pH on the stability of green synthesized MG–ZnO NPs. The pH stability of the nanoparticles was assessed using UV-Vis spectroscopy across a wide range of pH values, from 2 to 12. There were no distinct absorption peaks were observed between pH 2 and 7 (Fig. 7(a)), suggesting the instability of nanoparticles, possibly due to the protonation of the functional groups on phytochemicals, which may have hindered effective capping and stabilization. At pH 8, a sharp and well-defined peak appeared, indicating optimal stability under mildly alkaline conditions due to effective deprotonation of capping agents, which enhanced the nanoparticle stability. However, further increase in pH led to a gradual decrease in peak intensity, likely due to excess hydroxide ions interfering with surface interactions promoting the aggregation or partial dissolution of nanoparticles.[32]

3.4.2 Effect of various concentrations of NaCl on the stability of MG–ZnO NPs. The stability of the nanoparticles was further assessed by dispersing them in different concentrations of NaCl, ranging from 50 mM to 700 mM. A gradual decrease in the absorption peak intensity was observed (Fig. 7(b)),

indicating the destabilization of the nanoparticles with increasing NaCl concentration. This destabilization may be attributed to the screening of surfaces with Na^+ ions, which weakens electrostatic repulsion between particles and promotes aggregation.[32]

3.4.3 Effect of storage duration on the stability of MG–ZnO NPs. Finally, the effect of storage duration on the nanoparticle stability was analysed over a period of two months (5 days, 10 days, 15 days, 30 days, 45 days, 60 days). There was no noticeable decrease in the absorption peak intensity (Fig. 7(c)), indicating that the nanoparticles remained stable over long-term storage.

Stability studies under varying pH, salt concentrations, and storage durations are essential for assessing the suitability of nanoparticles in food packaging and preservation. MG–ZnO nanoparticles demonstrated excellent stability across these conditions, maintaining their structural integrity and functional properties. Their tolerance to high salt levels and a pH range, along with sustained stability over time, highlights their robustness in real-world food systems. These results position MG–ZnO NPs as strong candidates for incorporation into food-grade materials, offering long-lasting antimicrobial performance and environmental resilience.

3.5 Identification and characterization of the isolated microorganisms

A total of 12 distinct colonies were isolated and initially differentiated based on their morphological features such as shape, size, colour, and texture. Further, to screen the potential pathogenicity, a haemolysis test was performed using blood agar plates. Out of 12 isolates, 3 isolates have exhibited the haemolytic activity, one isolate exhibited β haemolysis by completely lysing the blood cells blood lysis and two other isolates showed the α haemolysis by partially lysing the blood cells while remaining 9 isolates displayed no haemolysis (γ haemolysis), indicating non-pathogenic nature. The three haemolytic isolates were further identified through 16S rRNA gene sequencing. As a result, the β haemolytic strain was identified as *Aeromonas caviae*, and other two α haemolytic strains were identified as *Staphylococcus pasteuri* and *Enterococcus faecalis*.

3.6 *In silico* studies

In silico studies were carried out using 32 ligands (Table S1) to assess their binding affinities with two key bacterial proteins: membrane bound transglycosylase (PDB ID : 3VMQ) and propyl endopeptidase (PDB ID : 3IUJ), associated with *Staphylococcus* spp. and *Aeromonas caviae*. These enzymes are essential for bacterial survival and pathogenicity. In both species, transglucosylases are involved in peptiglycan synthesis,[33] providing structural integrity to the cell wall and supporting the biofilm formation, which enhances the resistance to stress and antibiotics.[34]

3.6.1 Molecular docking with transglycosylase receptor (PDB ID : 3VMQ). *In silico* molecular docking studies were conducted using 32 ligands to assess their binding affinities with the selected target receptor (PDB ID : 3VMQ). Among these, seven
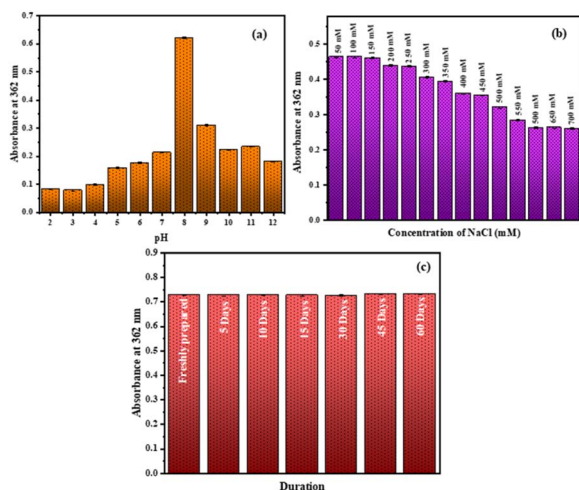

Fig. 7 UV-Vis Spectral graphs of MG–ZnO NPs stability studies, (a)-pH stability, (b)-concentration of NaCl, (c)-storage duration.
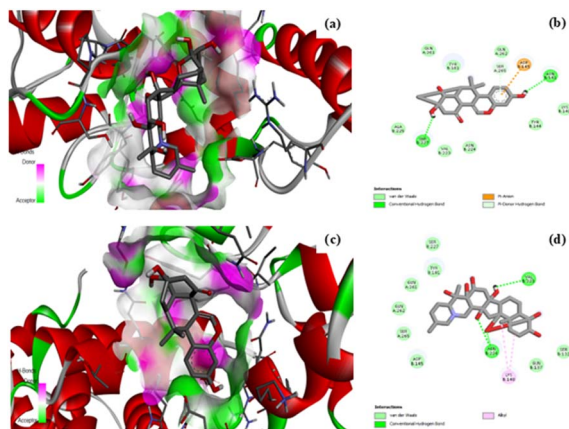
Fig. 8 Interaction of various ligands with 3VMQ, (a) and (b)-3D&2D structures of veracevine interaction; (c) and (d)-3D&2D structures of deoxymiroestrol interaction.

ligands exhibited notably strong binding interactions, with binding energies ranging from −7.1 to −8.1 kcal mol⁻¹, suggesting their potential as effective inhibitors. Detailed 2D interaction analysis revealed that these top ligands formed multiple conventional hydrogen bonds and hydrophobic interactions with key amino acid residues within the receptor's binding pocket (Table S7). Veracevine exhibited the strongest binding affinity (−8.1 kcal mol⁻¹), forming hydrogen bonds with Asn224 via the O1 and O2 atoms (3.06 Å and 2.23 Å), and with Val223 via the O5 atom (2.20 Å) (Fig. 8(a), (b) and Table 2). Deoxymiroestrol (−8.0 kcal mol⁻¹) formed hydrogen bonds with Ser227 and Asn141 through the O1 and O2 atoms at distances of 3.00 Å and 3.09 Å, respectively (Fig. 8(c), (d) and Table 2). 5-Deoxystrigol (−7.8 kcal mol⁻¹) interacted with Ser265 (O3 at 2.90 Å) and Tyr181 (O5 at 3.02 Å). Fustin (−7.6 kcal mol⁻¹) established hydrogen bonds with Asn141 (O3 at 3.74 Å) and Tyr181 (O1 at 3.06 Å). Dihydroisorhamnetin (−7.3 kcal mol⁻¹) formed hydrogen bonds with Tyr181 via the O6 and O2 atoms (2.74 Å and 3.34 Å), and with Asn141 via the O3 atom (3.23 Å). 3-Glucosyl-2,3′,4,4′,6-pentahydroxybenzophenone (−7.2 kcal mol⁻¹) exhibited extensive interactions, forming hydrogen bonds with Lys140 (O4 at 3.93 Å), Asn141 (O7 and O5 at 3.71 Å and 3.90 Å), Thr258 (O2 at 3.33 Å), Lys222 (O14 at 3.02 Å), and Asn224 (O13 at 3.79 Å). Chryso-obtusin (−7.1 kcal mol⁻¹) formed a hydrogen bond with Asn141 via the O3 atom at 2.83 Å. These interactions highlight the ability of the ligands to form stable and specific interactions with the receptor's site, supporting their potential role as antimicrobial agents.

3.6.2 Molecular docking with propyl endopeptidase receptor (PDB ID : 3IUJ). *In silico* molecular docking studies were performed using 32 ligands to evaluate their binding affinities with the target receptor (PDB ID : 3IUJ). Among these, ten ligands showed strong binding interactions, with binding energies ranging from −9.9 to −7.0 kcal mol⁻¹ (Table 2), indicating their potential as effective inhibitors. 2D interaction analysis revealed that these top ligands formed multiple conventional hydrogen bonds and hydrophobic interactions with key residues in the receptor's binding site (Table S8). Veracevine exhibited the strongest binding affinity (−9.9 kcal mol⁻¹), forming hydrogen bonds with Val238 (O5 at 3.03 Å), Thr239 (O6 at 3.01 Å), and Glu84 (O5 at 3.33 Å) (Fig. 9(a), (b) and Table 2). Deoxymiroestrol (−9.0 kcal mol⁻¹) formed hydrogen bonds with Arg135 (O1 at 3.08 Å), Glu240 (O3 at 3.03 Å), Asp285 (O6 at 2.90 Å), and Ser332 (O6 at 2.85 Å). 3-Glucosyl-2,3′,4,4′,6-pentahydroxybenzophenone (−8.2 kcal mol⁻¹) showed extensive interactions with Phe133 (O8, O10, O9 at 3.71 Å, 3.11 Å, 3.00 Å), Arg135 (O3 at 3.09 Å), Glu84 (O7 at 3.81 Å), Ser332 (O6 at 3.90 Å, 3.03 Å), and Val284 (O1 at 3.73 Å) (Fig. 9(c), (d) and Table 2). 5-Deoxystrigol (−8.1 kcal mol⁻¹) formed a hydrogen bond with Trp179 via O4 (2.94 Å). Dihydroisorhamnetin (−8.1 kcal mol⁻¹) interacted with Ser132 (O5 at 2.90 Å), Val284 (O3 at 3.00 Å), and Phe133 (O14 and O4 at 3.05 Å and 2.87 Å). Phloionolic acid (−7.6 kcal mol⁻¹) formed a bond with Arg135 (O1 at 3.27 Å). Fustin (−7.4 kcal mol⁻¹) showed hydrogen bonding with Glu240 (O8 at 3.57 Å), Val238 (O1 at 3.73 Å), and Phe133 (O4 at 3.94 Å and 3.96 Å). Chryso-obtusin (−7.2 kcal mol⁻¹) formed a bond with Ala80 (O5 at 3.09 Å). D-lactose (−7.2 kcal mol⁻¹) interacted with Gly375 (O1 and O11 at 3.21 Å and 2.83 Å) and Ser332 (O10 at 2.90 Å). L-1,2,3,4-tetrahydro-β-carboline-3-carboxylic acid (−7.0 kcal mol⁻¹) formed hydrogen bonds with Ser248 (O1 at 3.7 Å) and Phe174 (N3 at 3.2 Å). These interactions highlight the ability of the ligands to form stable and specific interactions with receptor's site, supporting their potential role as antimicrobial agents.

3.7 Minimal inhibition concentration (MIC) and minimum bactericidal concentration (MBC) determination

The MIC and MBC values of green synthesised MG-ZnO NPs were evaluated against the three strains: *Aeromonas caviae*, *Staphylococcus pasteuri* and *Enterococcus faecalis*. The bactericidal activity was not observed against *Enterococcus faecalis*, indicating resistance to the nanoparticles. In contrast, both *Aeromonas caviae* and *Staphylococcus pasteuri* showed significant sensitivity (Fig. 10). The MIC values of *Staphylococcus pasteuri* and *Aeromonas caviae* were 62.5 µg mL⁻¹ and 250 µg mL⁻¹

Table 2 Binding energies and interacting amino acid residues of selected ligands docked with target receptor proteins

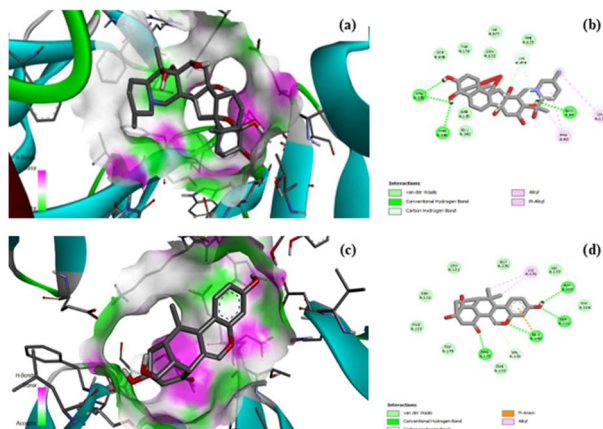|	Propyl endopeptidase		Transglycosylase	
Name of the ligand	Amino acids	Binding energy (kcal mol⁻¹)	Amino acids	Binding energy (kcal mol⁻¹)
Veracevin	Threonine, glutamic acid, valine, lysine	−9.9	Asparagine, valine	−8.1
Deoxymiroestrol	Arginine, glutamic acid, asparagine, serine, valine	−9.0	Serine, asparagine, serine	−8.0

Fig. 9 Interaction of various ligands with propyl endopeptidase receptor; (a) and (b)-3D&2D structures of veracevine interaction; (c) and (d)-3D&2D structures of deoxymiroestrol interaction.
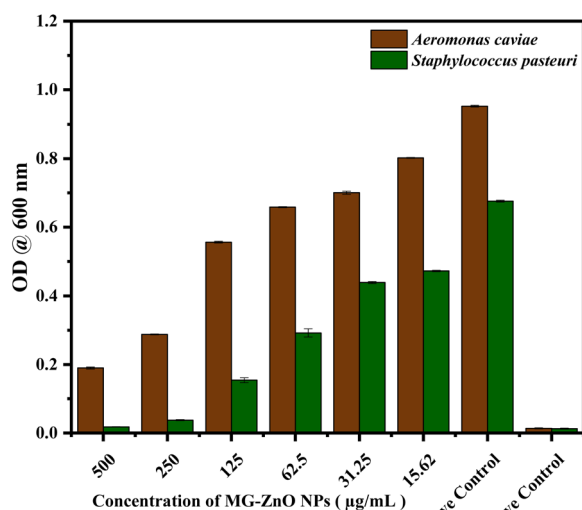

Fig. 10 Antimicrobial activity of MG-ZnO NPs against *Staphylococcus pasteuri* and *Aeromonas caviae*.

respectively, while the corresponding MBC values were 125 μg mL^{-1} and 500 μg mL^{-1}. The MBC/MIC ratios confirmed bactericidal efficacy of MG-ZnO NPs against these two strains. All the assays were performed in triplicate, and the results showed high reproducibility with minimal variation among replicates. One-way ANOVA analysis was conducted to statistically assess the variation across the triplicate sets. The results revealed no significant difference between replicates ($p < 0.05$), confirming the consistency and reproducibility.

3.8 Antibacterial mechanism of MG-ZnO NPs

Zinc oxide nanoparticles exhibit strong antimicrobial activity through multiple mechanisms that involve both physical and chemical interactions with bacterial cells (Fig. 11). One of the primary modes of action is the generation of reactive oxygen species (ROS) such as superoxide anions, hydroxyl radicals, and hydrogen peroxide. These ROS oxidative stress, which damages
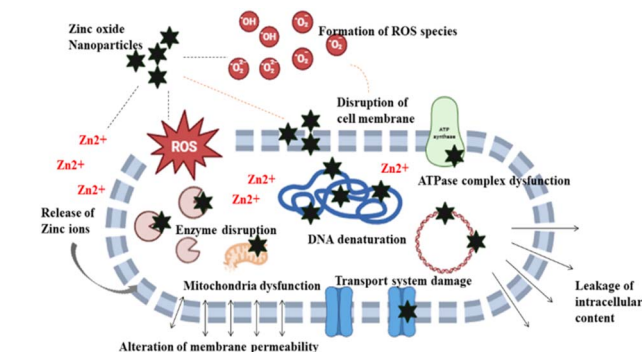

Fig. 11 Shematic representation of antibacterial activity of ZnO NPs.

bacterial lipids, leading to the cell wall disruption and eventually cell lysis.[35] ZnO NPs also interact electrostatically with bacterial membrane, resulting in membrane stability disruption, increasing permeability and causing leakage of vital cellular contents. In addition, the gradual release of Zn^{2+} ions from the nanoparticles further enhances their antimicrobial activity by interfering with essential enzymes, disrupting DNA replication, and causing protein denaturation. Furthermore, ZnO NPs can also penetrate bacterial cells and induce intracellular oxidative stress and damage critical cellular structures, contributing to bacterial inactivation.[36] Additionally, in green synthesised ZnO NPs, the use of plant extracts introduces bioactive compounds such as flavonoids, terpenoids, alkaloids, and phenolics. These phytochemicals when capped on the nanoparticle surface, enhances their antimicrobial activity through synergistic action.[37]

Conclusion

This study introduces a novel and eco-friendly strategy for synthesizing zinc oxide nanoparticles (ZnO NPs) using chia microgreens, highlighting their dual role as both a nutritional source and a green precursor for nanomaterials. LC-MS analysis confirmed the presence of diverse phytochemicals with known biological activity, and further *in silico* molecular docking studies demonstrated strong interactions between these compounds and essential bacterial proteins, suggesting their potential role in antimicrobial mechanisms. Utilizing the rich phytochemical profile of chia microgreens, ZnO NPs were successfully synthesized *via* a green synthesis. The resulting nanoparticles exhibited notable antibacterial activity against foodborne pathogens, with enhanced efficacy observed against *Staphylococcus pasteuri*. These findings underscore the potential of chia microgreens not only in sustainable nanoparticle synthesis but also in the development of effective antimicrobial agents for food safety and biomedical applications. However, the study is limited by the lack of detailed mechanistic insight into the antimicrobial action of the MG-ZnO NPs, as well as the absence of cytotoxicity and *in vivo* biocompatibility assessments. Future studies should focus on elucidating the mode of action, evaluating long-term safety, and exploring the practical integration of these nanoparticles into food packaging systems under real-world conditions.

Author contributions

Baru Venkata Naga Sahithi – conceptualization, methodology, software, formal analysis, data curation, writing – original draft, writing – review & editing, visualization, project administration. Vasantha V. L. – conceptualization, methodology, supervision, resources, writing – review & editing, project administration.

Conflicts of interest

The authors declare that there are no conflicts of interest.

Data availability

All the data supporting the findings of this study are included text, figures, and tables. Other supporting data is available in the supplementary data.

Supplementary information includes data on the characterization of chia microgreen extract, optimization of MG–ZnO nanoparticles, pathogenicity assay, and *in silico* interaction studies, presented in the form of tables and figures. See DOI: https://doi.org/10.1039/d5ra04728e.

Acknowledgements

References

1 M. Roselli, F. Natella, P. Zinno, B. Guantario, R. Canali, E. Schifano, M. De Angelis, O. Nikoloudaki, M. Gobbetti, G. Perozzi and C. Devirgiliis, *Front. Nutr.*, 2021, **8**, 689084.

2 F. Wang, W. Zhang and D. Niu, *Front. Cell. Infect. Microbiol.*, 2021, **11**, 772359.

3 N. Lyu, Y. Feng, Y. Pan, H. Huang, Y. Liu, C. Xue, B. Zhu and Y. Hu, *Front. Microbiol.*, 2021, **12**, 636332.

4 T. Bintsis, *AIMS Microbiol.*, 2017, **3**, 529–563.

5 U. Singh, *J. Food Prot.*, 1997, **60**, 125–130.

6 P. K. Praveen, C. Debnath, S. Shekhar, N. Dalai and S. Ganguly, *Vet. World*, 2016, **9**, 6–11.

7 O. Chesneau, A. Morvan, F. Grimont, H. Labischinski and N. el Solh, *Int. J. Syst. Bacteriol.*, 1993, **43**, 237–244.

8 J. Ramnarain, J. Yoon and N. Runnegar, *IDCases*, 2019, **18**, e00656.

9 V. Savini, C. Catavitello, D. Carlino, A. Bianco, A. Pompilio, A. Balbinot, R. Piccolomini, G. Di Bonaventura and D. D'Antonio, *J. Clin. Pathol.*, 2009, **62**, 957–958.

10 K. Fijałkowski, D. Peitler and J. Karakulska, *Int. J. Food Microbiol.*, 2016, **238**, 113–120.

11 M. L. Cohen, *Science*, 1992, **257**, 1050–1055.

12 J. Shin, V.-S. Prabhakaran and K.-S. Kim, *Microb. Pathog.*, 2018, **116**, 209–214.

13 P. Thakur and K. Kumar, *J. Agric. Eng. Food Technol.*, 2019, **6**, 155–160.

14 S. John, S. Gunathilake, S. Aluthge, A. Farahnaky and M. Majzoobi, *Food Bioprocess Technol.*, 2025, **18**, 5605–5620.

15 S. Motyka, H. Ekiert and A. Szopa, *Curr. Issues Pharm. Med. Sci.*, 2023, **36**, 33–43.

16 M. Bhaswant, D. K. Shanmugam, T. Miyazawa, C. Abe and T. Miyazawa, *Molecules*, 2023, **28**, 867.

17 G. Pal, P. Rai and A. Pandey, *Green Synth., Charact. Appl. Nanopart.*, 2019, 1–26.

18 K. Singh and S. Yadav, *Sci. Rep.*, 2025, **15**, 4043.

19 M. A. Ashkar, A. Babu, R. Joseph, S. Kutti Rani and N. Vasimalai, *Inorg. Chem. Commun.*, 2023, **156**, 111225.

20 H. Wu, M. Wang, Y. Liu, X. Wang, Y. Wang, J. Lu and H. Xu, *Int. J. Food Microbiol.*, 2016, **232**, 95–102.

21 M. S. Kumar, S. Pakrashy, S. Manna, S. M. Choudhury, B. Das, A. Ghosh, A. H. Seikh, M. Dolai and A. K. Das, *Anal. Methods*, 2025, **17**, 2125–2133.

22 M. Elshikh, S. Ahmed, S. Funston, P. Dunlop, M. McGaw, R. Marchant and I. M. Banat, *Biotechnol. Lett.*, 2016, **38**, 1015–1019.

23 T. Kokila, P. S. Ramesh and D. Geetha, *Appl. Nanosci.*, 2015, **5**, 911–920.

24 R. Ashraf, S. Riaz, S. S. Hussain and S. Naseem, *Mater. Today*, 2015, **2**, 5754–5759.

25 S. Yazdani, A. Daneshkhah, A. Diwate, H. Patel, J. Smith, O. Reul, R. Cheng, A. Izadian and A. R. Hajrasouliha, *ACS Omega*, 2021, **6**, 16847–16853.

26 A. Alam, M. Tabassum, S. Mostofa, R. Kumar Bishwas, D. Sarkar and S. Akter Jahan, *J. Cryst. Growth*, 2023, **621**, 127386.

27 N. Skandalis, A. Dimopoulou, A. Georgopoulou, N. Gallios, D. Papadopoulos, D. Tsipas, I. Theologidis, N. Michailidis and M. Chatzinikolaidou, *Nanomaterials*, 2017, **7**, 178.

28 S. W. Balogun, O. O. James, Y. K. Sanusi and O. H. Olayinka, *SN Appl. Sci.*, 2020, **2**, 504.

29 A. Fouda, E. Saied, A. M. Eid, F. Kouadri, A. M. Alemam, M. F. Hamza, M. Alharbi, A. Elkelish and S. E.-D. Hassan, *J. Funct. Biomater.*, 2023, **14**, 205.

30 S. Fakhari, M. Jamzad and H. Kabiri Fard, *Green Chem. Lett. Rev.*, 2019, **12**, 19–24.

31 R. Chokkareddy and G. G. Redhi, in *Green Metal Nanoparticles*, John Wiley & Sons, Inc., Hoboken, NJ, USA, 2018, pp. 113–139.

32 X. Wang, T. Sun, H. Zhu, T. Han, J. Wang and H. Dai, *J. Environ. Manage.*, 2020, **267**, 110656.

33 A. Galinier, C. Delan Forino, E. Foulquier, H. Lakhal and F. Pompeo, *Biomolecules*, 2023, **5**, 720.

34 I. G. Boneca, *Curr. Opin. Microbiol.*, 2005, **8**, 46–53.

35 B. Abebe, E. A. Zereffa, A. Tadesse and H. C. A. Murthy, *Nanoscale Res. Lett.*, 2020, **15**, 190.

36 A. Singh, N. B. Singh, S. Afzal, T. Singh and I. Hussain, *J. Mater. Sci.*, 2018, **53**, 185–201.

37 R. Díaz-Puertas, F. J. Álvarez-Martínez, A. Falcó, E. Barrajón-Catalán and R. Mallavia, *Polymers*, 2023, **15**, 1392.